HAL open science

Chaotic mixing in an acoustically driven cavity flow

Jingang Qu, Daniel Henry, Sophie Miralles, Valéry Botton, Florence Raynal

To cite this version:

Jingang Qu, Daniel Henry, Sophie Miralles, Valéry Botton, Florence Raynal. Chaotic mixing in an acoustically driven cavity flow. Physical Review Fluids, 2022, 7 (6), pp.064501. 10.1103/physrevfluids.7.064501 . hal-03693739

HAL Id: hal-03693739

https://hal.science/hal-03693739v1

Submitted on 13 Jun 2022

HAL is a multi-disciplinary open access archive for the deposit and dissemination of scientific research documents, whether they are published or not. The documents may come from teaching and research institutions in France or abroad, or from public or private research centers.

L'archive ouverte pluridisciplinaire **HAL**, est destinée au dépôt et à la diffusion de documents scientifiques de niveau recherche, publiés ou non, émanant des établissements d'enseignement et de recherche français ou étrangers, des laboratoires publics ou privés.

Chaotic mixing in an acoustically driven cavity flow

Jingang Qu, Daniel Henry, Sophie Miralles, Valéry Botton, and Florence Raynal
Laboratoire de Mécanique des Fluides et d'Acoustique, Univ Lyon, École centrale de Lyon, INSA Lyon, Univ Claude Bernard Lyon 1, CNRS, 69134 Écully Cédex, France

(Received 8 November 2021; accepted 25 May 2022; published 10 June 2022)

In this numerical study, we investigate the mixing properties of an acoustic driven flow in a parallelepipedic cavity with square basis in view of applications in photovoltaic crystal growth configurations. A single acoustic source is used, but, relying on non-normal reflections, an acoustic beam with a square path is obtained, generating a global complex flow in the cavity. Depending on the power of the source, the flow field may be steady, periodic in time, or chaotic. We restrict here on the steady and periodic cases and show that those flow fields enable chaotic advection. In the case of oscillating periodic flow fields, the chaotic region invades the whole cavity, as shown by numerical simulations of Poincaré sections and animations of mixing. This illustrates that acoustic streaming at moderate powers can be used successfully as a nonintrusive tool to mix efficiently.

DOI: 10.1103/PhysRevFluids.7.064501

I. INTRODUCTION

Acoustic streaming can be seen as a nonintrusive way to stir liquids and generate mixing in a number of processes ranging from microfluidics [1,2] to organic chemistry and food processing [3–5]. A number of former studies focused on mixing enhancement at very small scales [6,7]. But mixing at greater scales has also been considered, generally based on the possibility of creating jetlike flows. Since the pioneering works by Eckart, Lighthill, and Nyborg [8–10], a good knowledge of the scaling of such acoustic streaming flows occurring along a beam has been developed [11–13]. A possible configuration is to introduce an acoustic beam propagating along the cylinder axis, thus leading to a flow dominated by a possibly unstable vortex ring with downward velocity along the cylinder axis [14,15]. Interestingly, Ref. [16] also used several ultrasonic sources to increase the geometric complexity of the flow and generate chaotic mixing in a cylindrical container. Our team is interested in improving mixing in parallelepipedic cavities in connection with photovoltaic crystal growth configurations [17,18]. In this context, relying on non-normal reflections of an acoustic beam on the container walls makes it possible to generate several jets with a single acoustic source [19,20], thus leading to 3D flows prone to destabilize and even reach chaotic states [21,22] when increasing the acoustic power introduced in the liquid. But, even in the case of the steady flows observed at very low forcing, the geometric complexity of these flows could yield efficient Lagrangian mixing; this is the starting point of the present paper.

The ability of a given laminar flow field to generate chaotic trajectories was demonstrated by Aref [23]: He proved that a two-dimensional (2D) time-periodic flow produced by *blinking vortices* in perfect fluid could lead to efficient stirring, and named this phenomenon *chaotic advection*. Dombre *et al.* [24] extended this study to the case of three-dimensional (3D) steady flows with the ABC flows. The matter further triggered a great amount of theoretical, numerical, or experimental works on the subject (see, for instance, Refs. [25–33]). Note finally that chaotic advection also applies for dynamical systems of higher dimension, as, for instance, 3D time-periodic flows [34–38]. Chaotic

 ©2022 American Physical Society

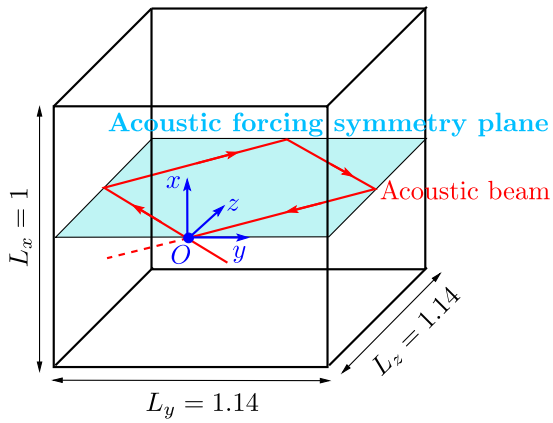

FIG. 1. Sketch of the configuration: The base of the cavity is square. The acoustic beam enters with an angle $\pi/4$, reflects on the walls, and leaves the cavity at the place where it entered.

advection has many fields of application in mixing, like microfluidics [39–41] or heat exchangers at the macroscale [42–44].

In this paper, we numerically investigate how acoustic streaming induces mixing in a parallelepipedic tank at the macroscale. While the acoustic forcing is essentially 2D, we show that the 3D-flow field produced is complex enough, even at low acoustic powers, to enable chaotic advection. At moderate acoustic powers, when the flow field becomes periodic in time in addition to 3D, chaos is global in the whole domain.

Note that in the following, we only consider the *dispersion* of a fluid particle by the velocity field, and we did not take into account the effects of molecular diffusion. Indeed, in liquids, molecular diffusion is very weak, so its effects in poorly mixing flows are visible on very long timescales [45]. In the case of chaotic mixing, the flow field is known to produce very thin scalar structures, which are rapidly mixed by molecular diffusion, at timescales of the order of the typical dispersion time [46].

II. NUMERICAL FLOW FIELD AND TRAJECTORIES

A. The acoustically driven flow

The flow field considered here is the acoustic streaming flow presented in Ref. [22] and corresponding to the experimental investigation by Cambonie *et al.* [21].

As shown in Fig. 1, it is created at midheight of a closed parallelepipedic cavity of square horizontal section, filled with water, by an acoustic beam emitted by a 2-MHz circular plane transducer of diameter 28.5 mm. This beam enters the cavity horizontally at the center of one of the vertical walls with an angle of $\pi/4$ and reflects successively on the three other vertical walls before leaving the cavity at the place where it entered, determining a square path at midheight of the cavity (see the comments on the choice of such a configuration in Ref. [47]).

As shown in Ref. [22], the flow is governed by the Navier-Stokes equations with a force term corresponding to the acoustic forcing. To make these equations dimensionless, we choose the height of the cavity H as reference length, and we introduce a reference viscous time H^2/ν, where ν is the kinematic viscosity of the fluid, and a reference pressure $\rho\nu^2/H^2$ with ρ the fluid density. The acoustic force can thus be expressed as

$$\mathbf{F}(x, y, z) = 4\,A\,I(x, y, z)\,\mathbf{e}_p, \tag{1}$$

where $I(x, y, z)$ is the normalized acoustic intensity distribution, $\mathbf{e}_p$ is the acoustic beam direction of propagation, and A is the acoustic streaming parameter defined as

$$A = \frac{2\alpha P_{\mathrm{ac}} H^3}{\pi\, c\, R_t^2\, \rho\, \nu^2}. \tag{2}$$

In this expression, α is the acoustic attenuation (m^{-1}), P_{ac} is the acoustic power delivered by the transducer (W), c is the sound velocity, and R_t is the transducer radius. For the parameters of the experiment by Cambonie *et al.* [21] (i.e., $\alpha = 0.1\ \mathrm{m}^{-1}$, $\rho = 10^3\,\mathrm{kg/m^3}$, $c = 1480\ \mathrm{m/s}$, $\nu = 9.3 \times 10^{-7}\,\mathrm{m^2/s}$, $R_t = 0.01425$ m, and $H = 0.16$ m), $A = 10^6$ corresponds to a dimensional power $P_{\mathrm{ac}} = 1$ W. The reference time is 27 500 s and the reference velocity, expressed as ν/H, is $5.8 \times 10^{-6}\,\mathrm{m/s}$. The normalized acoustic intensity distribution $I(x, y, z)$ in the cavity is computed for the above parameters by means of the Rayleigh integral for each beam (see Eq. (5) in Ref. [19] and the normalization in Ref. [22], based on Ref. [48]). The cavity (which corresponds here to the experiment by Cambonie *et al.* [21]) has dimensionless size 1 along x (from -0.5 to 0.5) in the vertical direction, 1.14 along y (from -0.57 to 0.57) and 1.14 along z (from 0 to 1.14) (square horizontal cross section), and the acoustic streaming flow is forced at midheight (i.e., at mid-x), while the beam enters the cavity at mid-y. No-slip boundary is applied at the walls.

The numerical flow field used to compute the trajectories is obtained by unsteady simulations with a spectral finite-element code [22,49]. The grid comprises two elements in the vertical direction (with 21 points per element) and two elements in each of the two horizontal directions (with 31 points per element), which gives $41 \times 61 \times 61$ grid points in the $x \times y \times z$ directions. It was shown in Ref. [22] that this grid provides a good discretization of the imposed acoustic forcing and a good precision for the calculation of the flow.

The acoustic streaming parameter A is varied from 10^4 to 2.4×10^6. The flows at $A = 10^4$, 10^5, and 10^6 are steady. The flows at $A = 1.5 \times 10^6$, 2×10^6, and 2.4×10^6 are oscillatory periodic. Note that, because of the divergence and attenuation of the acoustic beam considered in the calculation of the acoustic intensity, the forcing is different in the four branches of the acoustic beam, preventing any exact symmetry on the velocity field to occur between these branches. The only possible symmetry in this configuration is the up-down symmetry about the mid-x plane ($x = 0$). This symmetry is found to be effective in the steady flows, but it is broken in the oscillatory periodic flows.

To characterize the flow, it is usual to define a Reynolds number of the flow, $\mathrm{Re} = V\,H/\nu$, based on a reference velocity V (here, Re is simply the nondimensional velocity). In this flow, there is no obvious choice for the reference velocity, so we propose three different choices: one based on the maximum of velocity in the flow, the second on the average velocity in the midheight horizontal plane where the acoustic ray is located, and the third based on the average velocity in the tank. As can be seen in Fig. 2(a), the three Reynolds numbers are quite proportional to one another and behave similarly with A. Using dimensional analysis, Ref. [12] showed that the velocity field in the acoustic beam scales with the acoustic streaming parameter A in the viscous regime (Stokes range) and as $A^{1/2}$ in the inertial range. The cases studied here are obviously in an intermediate range, where the velocity field is no more proportional to A, but not yet in the inertial range. We more precisely checked that the flow remains in the viscous regime, with a linear variation of its intensity with A, up to $A = 10^3$. Inertial effects are then perceptible for $A = 10^4$ and further amplified for larger values of A.

In parallel with the increase of the flow intensity, the width of the acoustic jets seems to decrease with A [see, for instance, Figs. 3(a)–3(c) in the horizontal midplane, and Figs. 3(d)–3(f) in a vertical plane], favoring larger velocity gradients. We can evaluate quantitatively this effect using the shear rate $|\dot{\gamma}| = \sqrt{0.5(\partial u_i/\partial x_j + \partial u_j/\partial x_i)^2}$; this quantity is maximum in the jet where it roughly features the ratio of the jet velocity to its width. Interestingly, this maximum shear rate remains reasonably proportional to A in the range of A studied, as shown in Fig. 2(b). Because the maximum velocity fails the proportionality with A at large values of the acoustic streaming parameter [Fig. 2(b)], this

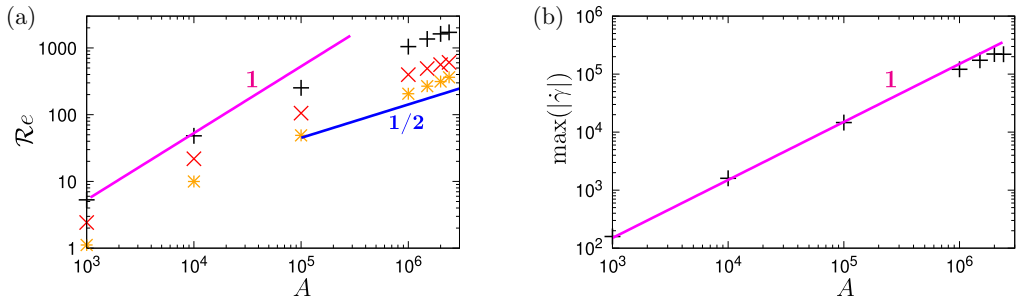

FIG. 2. (a) Reynolds number of the flow, $\mathrm{Re} = V\,H/\nu$, as a function of the acoustic streaming parameter A, based on different reference velocities V: $+$: maximum velocity in the flow; $\times$: average velocity in the horizontal midheight plane where the acoustic ray is located; $*$: averaged velocity in the whole tank. For the cases considered in the following ($A \geqslant 10^4$), inertial effects are clearly present, and become non-negligible for $A \geqslant 10^5$. (b) Maximum shear rate $|\dot{\gamma}| = \sqrt{0.5(\partial u_i/\partial x_j + \partial u_j/\partial x_i)^2}$ in the flow as a function of A. The dash-dotted line has equation $\max(|\dot{\gamma}|) = 0.15 \times A$. Unlike the maximum velocity, the maximum shear rate is fairly proportional to the acoustic streaming parameter A on the whole range of A.

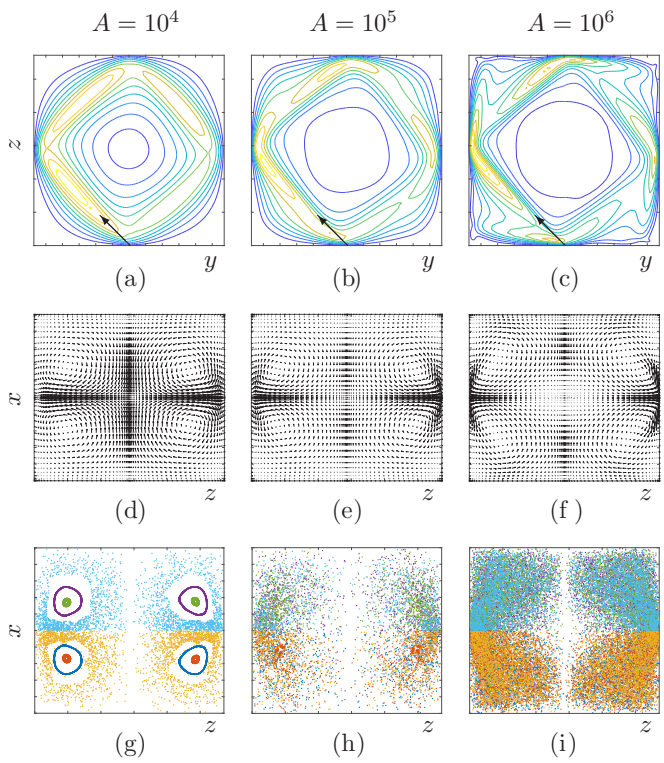

FIG. 3. Plots for the acoustic streaming steady flows. Left column: $A = 10^4$, middle column: $A = 10^5$, right column: $A = 10^6$. Top views: Isocontours of the horizontal velocity norm in the horizontal yz plane at mid-x. The step between the contours is constant: Nine contours between 5 and 45 in (a), eight contours between 30 and 240 in (b), ten contours between 100 and 1000 in (c). The arrows indicate the direction of the entering acoustic beam. Middle views: Velocity field in the vertical zx plane at mid-y. Bottom views: Poincaré sections in the zx plane at mid-y. We considered six initial points $(-0.25, 0.2, 0.3)$, $(-0.175, 0., 0.2)$, $(-0.1, 0., 0.45)$, and $(0.25, 0.2, 0.3)$, $(0.175, 0., 0.2)$, $(0.1, 0., 0.45)$, and the evolution time is $t = 50$.

implies that the width of the jet is roughly constant for small A and decreases when inertial effects come into play ($A > 10^4$).

B. Trajectories of tracers

The calculations of the trajectories of tracers for the different acoustic streaming cases are performed using MATLAB, with the solver function ode45 which adapts the time step to the required precision. Moreover, because the flow field is calculated on a grid, and stored at given instants in the case of time-periodic flows (49 instants for $A = 1.5 \times 10^6$ and 97 instants for $A = 2 \times 10^6$ and 2.4×10^6), we need to interpolate in space and time our original data. This is done using MATLAB function griddedInterpolant. This interpolation function and the precision needed in ode45 were tested on analytical flows, either steady or time periodic (see Appendixes A and B for the validation of the method). The precision finally chosen for the acoustic streaming cases was of 10^{-6}, a better precision (down to 10^{-10}) requiring more computational time, but not changing the results.

C. Tools of chaos: Poincaré sections and Lyapunov exponents

A *Poincaré section* of a dynamical system is the ensemble of points formed by the intersection of a given trajectory (or a few of them) with a lower-dimensional subspace. For all cases considered thereafter (either 3D steady flows or 3D time-periodic flows), the Poincaré sections chosen are vertical or horizontal planes located at the center of the box; for vertical Poincaré sections, we only show the zx plane located at mid-y, because the Poincaré sections are very similar to what is observed in other vertical planes, as the mid yx plane.

The *Lyapunov exponent* characterizes the exponential rate of separation of infinitesimally close trajectories. In the case of 3D flows, there are three Lyapunov exponents and the sum of those exponents is zero if the flow is incompressible, as in our case. If the flow is steady, the trajectories and streamlines coincide; therefore, one of the exponents is zero since two points on the same streamline never separate exponentially and the two other Lyapunov exponents have equal moduli and opposite signs. When the flow is both 3D and time periodic, there can be three nonzero Lyapunov exponents, the sum of them being still zero because of incompressibility.

In practice, Poincaré sections and Lyapunov exponents are calculated together. Note that because *very few initial points are considered*, trajectories have to be followed on a very long time so as to have enough intersection points for the Poincaré sections. This also ensures that the Lyapunov exponents are sufficiently converged. Therefore, the times considered for the calculation of those quantities are *orders of magnitude higher* than the typical time needed for dispersing many tracers initially located in a spot, as shown in the three videos of blob dispersion given in the Supplemental Material (see the discussion later in Sec. V).

III. LOW ACOUSTIC POWERS: 3D STEADY FLOWS

We first discuss the case of low acoustic powers, corresponding here to an acoustic streaming parameter A in between 10^4 and 10^6. In those cases, the flow is steady, and symmetric with respect to the mid-x horizontal plane. Therefore, the velocity has no vertical component in this plane, so trajectories can never cross this plane, and remain forever in their initial half of the cavity, either top or bottom. Figures 3(a)–3(c) show the norm of the velocity field in this horizontal plane for increasing values of the acoustic streaming parameter A. The global velocity field in the cavity has its maximums in this plane. In fact, four maximums are obtained, connected with the acceleration experienced in each portion of the acoustic beam. For the smallest value of A ($A = 10^4$), no inertial phenomenon is visible, and the main flow follows the beam trajectory, giving a rather circular flow pattern. When A is increased, inertial effects become visible and the patterns invade the corners of the cavity. For the largest value of A shown [Fig. 3(c)], the main flow consists of jets which impinge

on the walls of the cavity and flow further along these walls by inertia. In any case, a global rotation of the fluid about the vertical axis is induced in the whole cavity.

3D characteristics of the flows can also be obtained by looking in a vertical plane: Figs. 3(d)–3(f) show the velocity field in the zx plane at mid-y for the same values of the acoustic streaming parameter (similar velocity fields are obtained in the yx plane at mid-z). Note first that the up-down symmetry is visible in this plane for the three cases. For the smallest acoustic power corresponding to $A = 10^4$ [Fig. 3(d)], the flow has a cellular structure with four vortices. The fluid flows toward the horizontal midheight plane all around the central vertical axis and flows back along the vertical boundaries. This flow structure is a consequence of the depression created at the center of the acoustically induced rotating flow in the horizontal midheight plane. When A is increased [Figs. 3(e)–3(f)], these structures are modified by the impinging jets, which create flows on both sides of the midheight plane by inertia. The shape of the vortices is thus changed, the flow toward the midheight plane occurring obliquely in the direction of the impinged zone rather than vertically. The center of the vortices is also displaced closer to the vertical walls.

Trajectories issued from six different points have been calculated for these three steady cases. In Figs. 3(g)–3(i), we show the corresponding Poincaré sections in the vertical zx plane at mid-y. For $A = 10^4$ [Fig. 3(g)], we recover the vortical structures shown in the velocity field in this plane, here corresponding to four regular elliptic regions. In 3D, those regions are connected in pairs into two donut-shaped regions, symmetrical to each other with respect to the midheight horizontal plane where the acoustic forcing is imposed. Inside those structures, the trajectories are essentially regular, as visible in the figure where four of the initial points out of six were located inside those domains. Mixing between the fluid inside those structures and outside can only occur through diffusion, that is, at a timescale much larger than what can be expected in chaotic regions [45]. Outside those structures, the chaotic trajectories wander in their half plane, as expected from the up-down symmetry of the flow field.

For $A = 10^5$ [Fig. 3(h)], a sticky region (region where points remain for a while [50]) is still visible in the vicinity of the former regular region at $A = 10^4$; for $A = 10^6$ [Fig. 3(i)], regular and sticky regions have completely disappeared. The region around the central vertical axis (at mid-z in the picture), which is less visited, corresponds to zones at the center of the acoustically induced global rotation where the velocity perpendicular to the plane vanishes: the fluid particles will then rarely cross the Poincaré section at those locations. For all those Poincaré sections, we kept the total evolution time $t = 50$. Therefore, because the characteristic velocity is about four times more important for $A = 10^6$ than for $A = 10^5$ (see Fig. 2), the number of points in Fig. 3(i) is about four times higher than in Fig. 3(h).

Note that although the fluid particles do not cross the horizontal midheight plane in theses cases, mixing between the upper and lower halves of the cavity can occur in practice when taking into account molecular diffusion; however, as already explained, this mechanism is not efficient.

The evolution of the Lyapunov exponents corresponding to the trajectories obtained from three initial points [those from Figs. 3(g)–3(i) that are located in the lower half of the cavity] is finally shown for these steady cases in Fig. 4. As expected for a 3D steady flow, for each trajectory, one of the three Lyapunov exponents is zero. For $A = 10^4$ [Fig. 4(a)], two of the three initial points were taken in the regular regions, and their corresponding Lyapunov exponents go to zero. For the two higher values of A [$A = 10^5$ in Fig. 4(b)], the Lyapunov exponents converge to the same values whatever the initial point considered, which is expected for points located in the same chaotic region. Note also that the positive Lyapunov exponent is all the more important as the acoustic streaming parameter is high. We will come back to this point later, when also considering even higher acoustic powers.

IV. MODERATE ACOUSTIC POWERS: 3D OSCILLATORY PERIODIC FLOWS

When the acoustic streaming parameter A is further increased, the flow field becomes time dependent [21,22]. A first supercritical Hopf bifurcation occurs, leading for $A = 1.5 \times 10^6$ to an

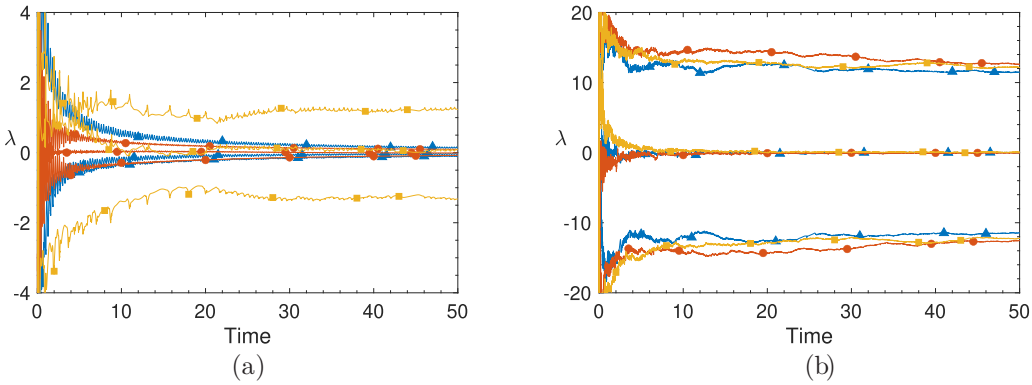

FIG. 4. Lyapunov exponents λ as a function of time obtained with trajectories issued from three different initial points for the acoustic streaming steady flows at $A = 10^4$ (a) and $A = 10^5$ (b). The points considered are ▲: (−0.25, 0.2, 0.3); •: (−0.175, 0., 0.2); ■: (−0.1, 0., 0.45); the colors are matching those in Figs. 3(g)–3(i).

oscillatory periodic flow with a period $T \approx 0.0065$. A period doubling is then observed, leading to a periodic state with an increased period ($T \approx 0.0105$) for $A = 2 \times 10^6$. A chaotic flow window then appears for A between 2.2×10^6 and 2.3×10^6, before a return to an oscillatory periodic flow for $A = 2.4 \times 10^6$, but with a smaller period than before ($T \approx 0.0040$). Finally, beyond this value of A, the time periodicity is lost and progressively more chaotic flows are obtained [22]. In the following, we restrict our study to cases where the flow field is oscillatory periodic, i.e., the cases at $A = 1.5 \times 10^6$, 2×10^6, and 2.4×10^6.

In such oscillatory situations, the flow field can be decomposed into a nonfluctuating part (the time-averaged flow, thereafter called the *base flow*) and a fluctuation. For $A = 1.5 \times 10^6$, while the base flow still shows the up-down symmetry, the time-dependent fluctuation breaks this symmetry, so the global oscillatory periodic flow is no more symmetric. The corresponding root mean square (rms) values of the fluctuation of the horizontal velocity norm in the midheight horizontal plane are shown in Fig. 5(a). Although much smaller in amplitude than the base flow (maximum value of about 100 compared to 1000 for the base flow), the fluctuation is highest in regions between the acoustic jets and the walls, avoiding the trapping of the fluid particles near the walls and in the

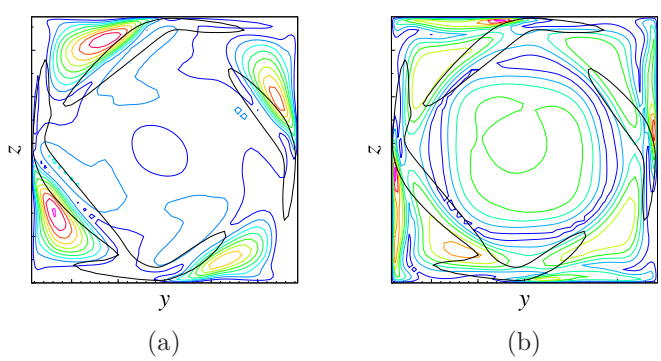

FIG. 5. Isocontours of the rms velocity fluctuation in the midheight horizontal plane for the oscillatory periodic case at $A = 1.5 \times 10^6$ ($T \approx 0.0065$). (a) rms values for the horizontal velocity norm; (b) rms values for the vertical (crossing) velocity. The step between the contours is constant and equal to 10, starting from the contour at 10 close to the walls where the value is 0. The thick black contour associated with the value 700 of the horizontal velocity norm for the base flow gives the location of the base flow jets in this case.

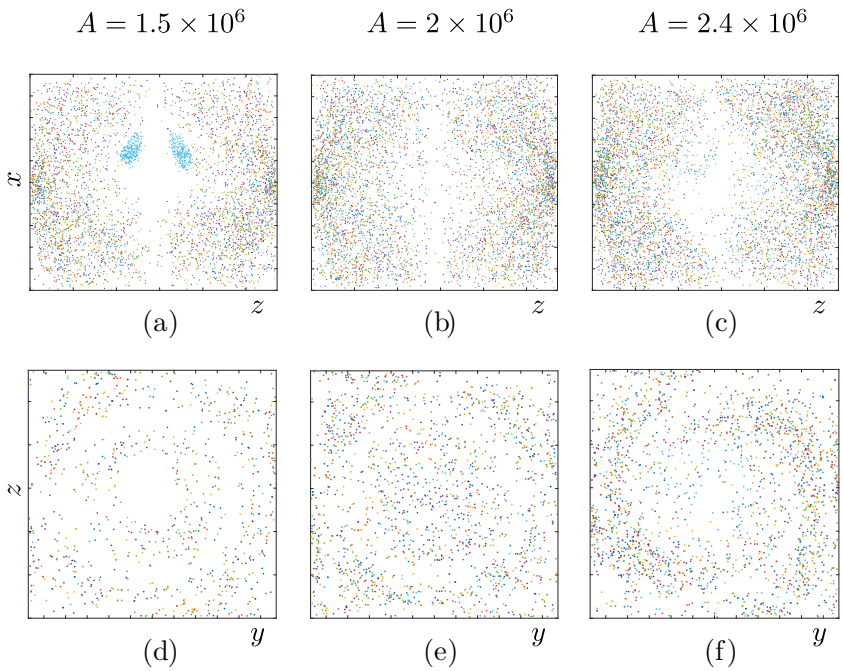

FIG. 6. Poincaré sections in different planes for the acoustic streaming periodic flows obtained at different values of parameter A. Left column: $A = 1.5 \times 10^6$, $T = 0.0065$; middle column: $A = 2 \times 10^6$, $T = 0.0105$; right column: $A = 2.4 \times 10^6$, $T = 0.0040$. The top views concern the vertical zx plane at mid-y and the bottom views the horizontal yz plane at mid-x. For all those sections, the six initial points considered are those given in Figs. 3(g)–3(i) (the evolution time of the trajectories is $t = 5$).

corners [51–54]. The rms values of the *vertical component* of the velocity in the same horizontal plane is also shown in Fig. 5(b): Although slightly smaller than the horizontal fluctuation, the vertical fluctuation now allows fluid particles to cross between the upper and lower halves of the cavity, even in the absence of molecular diffusion. Similar properties are found in the periodic case at $A = 2 \times 10^6$. For the periodic case at $A = 2.4 \times 10^6$, which occurs after a chaotic flow window at smaller A, even the base flow has already lost the up-down symmetry.

This loss of the up-down symmetry indeed affects the vertical Poincaré sections, as shown in Figs. 6(a)–6(c): The fluid particles now wander from the top half to the bottom half and reversely, whatever the periodic state considered ($A = 1.5 \times 10^6$, 2×10^6, and 2.4×10^6). The blue region in Fig. 6(a) corresponds to a fluid particle that remains for a while in the vicinity of a given trajectory, but escapes eventually after some time; thus, this is not a regular region as that shown in Fig. 3(g). For the larger acoustic streaming parameters considered here [Figs. 6(b) and 6(c), corresponding, respectively, to $A = 2 \times 10^6$ and 2.4×10^6], we did not find any such regions: Indeed, the points in the vertical Poincaré sections are rather well distributed in the whole surface, except for the region around the central vertical axis where the normal velocity is weak and which appears as nearly empty, and the vicinity of the acoustic jet (along the vertical boundaries at mid-x) where the velocity is highest and which is more populated.

Figures 6(d)–6(f) show the horizontal Poincaré sections for the same initial points and acoustic streaming parameters as above. As expected, those sections are less populated than the vertical sections, since the oscillating vertical flow allowing the fluid particles to cross this plane is much less intense than the base flow which is responsible for the global rotation in the cavity. In Fig. 6(d), we recognize the nearly circular less populated region, which corresponds to the region where the rms values of the vertical fluctuation are weak in Fig. 5(b).

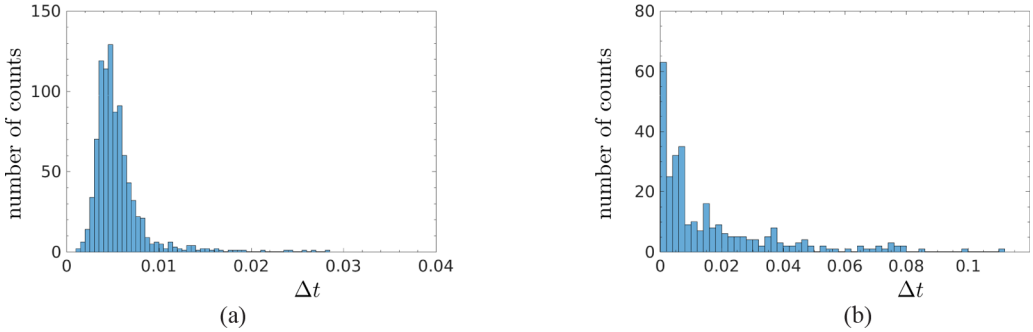

FIG. 7. Histograms of the time intervals Δt between crossings of a Poincaré plane for a single trajectory [initial point $(-0.25, 0.2, 0.3)$] for the oscillatory flow corresponding to $A = 2 \times 10^6$ ($T = 0.0105$). (a) vertical zx plane at mid-y; (b) horizontal yz plane at mid-x.

When comparing vertical and horizontal Poincaré sections, it is also interesting to consider the time intervals between crossings of a Poincaré section (also called *waiting time* [55] or *time of flight* [53]). Figure 7 shows the histograms of those times for the vertical and horizontal Poincaré sections at $A = 2 \times 10^6$ [Figs. 6(b) and 6(e)]. As expected, the number of counts is much larger for the vertical Poincaré plane [Fig. 7(a)] than for the horizontal plane [Fig. 7(b)] [the maximum number of counts in a bin is twice more in Fig. 7(a) than in Fig. 7(b); the five more populated bins have above 80 counts in Fig. 7(a) compared to only 10 in Fig. 7(b)]. The shapes of the two distributions are also very different: In the case of the vertical Poincaré plane, the distribution is peaked around a time of flight $\Delta t = 0.00475$ corresponding to a typical travel time with the base flow. For example, a typical length for half a rotation is about 1, and in the midheight plane where the maximum velocity is about 1600, the mean velocity is about 500 (see Fig. 2), which gives a travel time of $\Delta t = 0.002$. This is a good order of magnitude. Moreover, most trajectories are, in fact, outside this midheight plane, in regions of smaller velocities, which explains the somewhat larger travel time found. Note that in all three oscillatory flows studied here, the period T of the flow is of the same order as the typical timescale of the flow Δt. Therefore, we expect this oscillatory flow to be very efficient for spreading uniformly in the domain [56]. Indeed, the points in the vertical Poincaré sections are much more homogeneously distributed in the oscillating cases [Figs. 6(a)–6(c)] than in the steady cases [Figs. 3(g)–3(i)]. In contrast, for the horizontal Poincaré plane, the most probable travel time value is zero; this can be explained by the fact that the base flow is parallel to this plane at midheight and only the weak oscillating flow allows crossing it, thus creating a lot of almost tangent trajectories.

Finally, the Lyapunov exponents for the oscillatory periodic flows are displayed in Fig. 8. Because the velocity has a small oscillatory component, the intermediate exponent is not zero, but slightly positive. Interestingly here, while those simple laminar flows have only undergone a few bifurcations, we recover the same positive sign for the intermediate exponent as what has always been found in turbulent flows [57]. Once again, the highest positive exponent increases with the acoustic streaming parameter. The dependence of the largest positive Lyapunov exponent $\lambda_{\max}$ with the parameter A for all the cases considered in this study is shown in Fig. 9: In the range of A studied corresponding to nonchaotic velocity fields (either steady or time periodic), the Lyapunov exponent is found to be quite well proportional to A. To explain this behavior, it is first interesting to note that, from dimensional analysis, the Lyapunov exponent scales as a velocity gradient. As shown in Fig. 2(a), the typical velocity increases less rapidly than A outside the Stokes range, when inertial effects come into play. But, in parallel, the jet tends to become thinner, so the maximum velocity gradient remains approximately proportional to A, as illustrated through the shear rate in Fig. 2(b). We can then finally conjecture that the proportionality of the maximum Lyapunov exponent with A is due to the fact that it scales like the maximum velocity gradient in the jet.

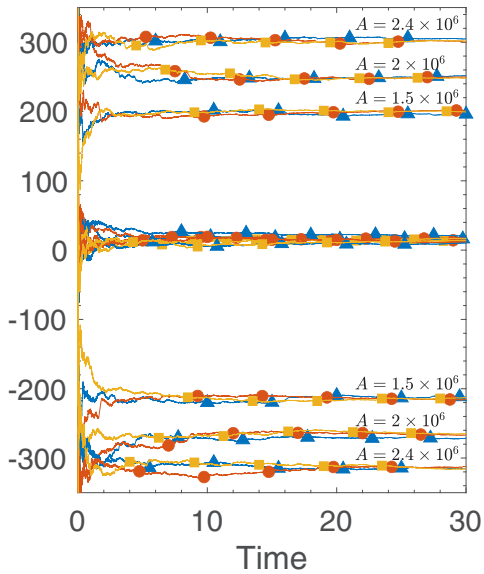

FIG. 8. Lyapunov exponents obtained with trajectories issued from three different initial points for the acoustic streaming oscillatory flows at $A = 1.5 \times 10^6$, $A = 2 \times 10^6$, and $A = 2.4 \times 10^6$. The points are those already used in Fig. 4: ▲: (−0.25, 0.2, 0.3); •: (−0.175, 0., 0.2); ■: (−0.1, 0., 0.45). In all cases, the intermediate Lyapunov exponent is slightly positive.

V. SUMMARY AND DISCUSSION

In this paper, we have studied the chaotic properties of trajectories issued from an acoustically driven laminar flow. At low acoustic powers, the flow field is 3D and steady: If the spreading of fluid particles is limited by the presence of regular islands for the lowest powers, we have also shown that, in any case, an up-down symmetry exists, which prevents mixing between the upper and bottom halves of the cavity. At moderate powers, the flow field becomes time dependent. We restricted our study to cases with time-periodic dependence, and showed that the oscillatory part not only enables a more homogeneous spreading of the fluid particles but also breaks the up-down symmetry: Trajectories can thus cross the midheight horizontal plane, allowing paths between the upper and lower halves of the cavity, as shown in Fig. 10. In that figure, the trajectories were

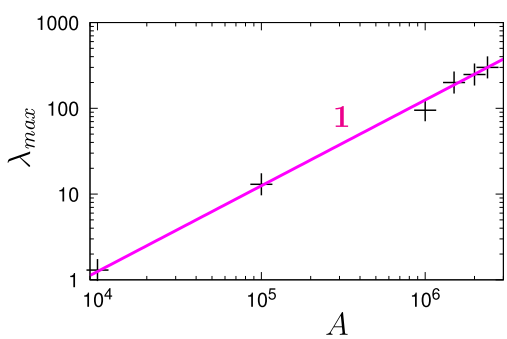

FIG. 9. Maximum positive Lyapunov exponent $\lambda_{\max}$ as a function of the acoustic streaming parameter A (log-log plot because of the large range of parameters). The fit is linear, with equation $\lambda = 1.25 \times 10^{-4} \times A$; the Lyapunov exponent is fairly proportional to A on more than two decades.

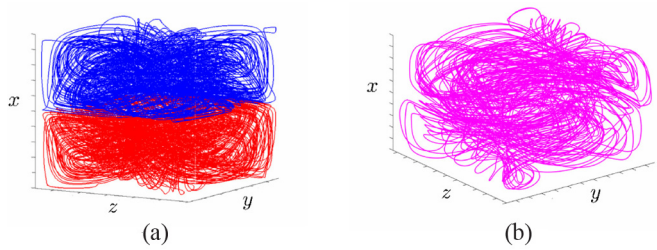

FIG. 10. (a) Steady flow at $A = 10^6$: Trajectories issued from symmetric points in the lower and upper halves of the cavity [(−0.25, 0.2, 0.3) and (0.25, 0.2, 0.3)]. Each trajectory remains in its half part, showing the very good up-down symmetry for those steady flows. The evolution time of the trajectories is $t = 3$. (b) Oscillatory flow at $A = 1.5 \times 10^6$: trajectory issued from the point (−0.25, 0.2, 0.3) in the lower half part of the cavity. The evolution time of the trajectory is $t = 5$.

followed for a dimensionless time $t = 3$ for the steady case at $A = 10^6$ [Fig. 10(a)] and $t = 5$ for the oscillatory case at $A = 1.5 \times 10^6$ [Fig. 10(b)]. These may seem very long times: Indeed, when brought back to the case of the experiment depicted in Sec. II, dimensional times of about 1 day and 1.5 days, respectively, are obtained. In practice, however, mixing does not consist of following a single trajectory, but rather a large number of fluid particles, generally initially released together at some place in the flow: The particles begin to separate from each other at a typical timescale of the order of the inverse of the Lyapunov exponent. Typically, for a blob of size ℓ submitted to an exponential stretching characterized by a positive exponent λ, the blob is considered as stretched macroscopically when its size reaches the size of the container L, at a time $t_{\text{macro}} \approx (1/\lambda)\ln(L/\ell)$, and is rapidly mixed thereafter. .

As an illustration, we show three videos of mixing in those flows as Supplemental Material, two of which corresponding to the cases depicted in Fig. 10 (steady flow at $A = 10^6$ [58] and oscillatory flow at $A = 1.5 \times 10^6$ [59]), and the last one being the oscillatory case at $A = 2.4 \times 10^6$ [60]. The blob of dye to be mixed consists of a little cube of size 0.001, which contains 1331 particles (11 points in each direction of space), initially located at a given point of space [(−0.25, 0.2, 0.3), the same for all videos]. The particles are represented by circles so as to be more visible (the particles are at the center of the circles). The positions of the particles are sampled every 10^{-3} instants; there are 120 such instants in the steady case at $A = 10^6$ (total time $t = 0.12$, which corresponds to a dimensional time less than an hour), while in the periodic cases, 50 instants are given for a total time $t = 0.05$ (around 20 min in dimensional time). For the three videos, given the size of the blob and taking $L = H$, we have t_{macro} approximately equal to 0.07 ($A = 10^6$), 0.03 ($A = 1.5 \times 10^6$), and 0.02 ($A = 2.4 \times 10^6$). As already pointed out in Sec. II C, those times are *orders of magnitude smaller* than the times needed to build a Poincaré section; for illustrative purposes, those times would correspond to 32, 14, and 9 min, respectively, in dimensional time. In all cases, t_{macro} is less than the total time represented on the videos, although of the same order of magnitude (see the comments on the videos in Ref. [61]). In the oscillatory cases, the total time was enough to see a complete dispersion of the fluid particles in the whole space.

One could wonder whether there is a particular interest in using acoustic streaming for mixing in a tank of *macroscopic* size. First, as already noticed, acoustic is a nonintrusive method to create a flow field: Therefore, it could be used in processes where the absence of impurities is a technological issue. Another scientific challenge is the case of crystallization processes. If chaotic advection was shown to speed up crystallization in natural conditions like solidification of magma [62], what are the possibilities in industrial processes? Chaotic advection induced by acoustic streaming could be used, for instance, in the directional solidification processes for photovoltaic silicon purification, which is an important issue since the presence of impurities strongly impacts solar cells efficiency [63]. In such processes, an efficient mixing in the liquid phase is required to sweep the impurities from the solid-liquid interface and homogenize the liquid phase.

Chatelain *et al.* [18] studied the possibility to use a mechanical stirrer. The moving solid-liquid front, however, renders difficult the introduction of a mechanical stirrer, which would have to be progressively removed from the tank. Other complexities lie in the fact that the stirrer has to resist to strong temperatures, and also that there is a risk of impurities release during the process. To cope with these problems, the use of acoustic streaming is a real alternative. The velocities obtained by acoustic streaming are indeed smaller than those obtained with the stirrer (about 1 cm/s compared with several cm/s). The solidification front velocity is, however, very weak in directional solidification ($v_{\text{front}} \sim 10^{-3}$cm/s [18]), so the typical timescales found in this study afford the possibility of using chaotic advection produced by acoustic streaming for mixing in this type of technology.

ACKNOWLEDGMENTS

The authors wish to thank Veaceslav Goian for his preliminary work on the problem. This work was carried out as part of the BRASSOA project supported by the institut Carnot Ingénierie@Lyon and of the PHC Maghreb Partnership Program No. 36951NG. The support from the PMCS2I of École Centrale de Lyon for the numerical calculations is also gratefully acknowledged. We particularly thank Laurent Pouilloux for advice and great availability at any stage of our project. We also thank an anonymous referee for interesting comments.

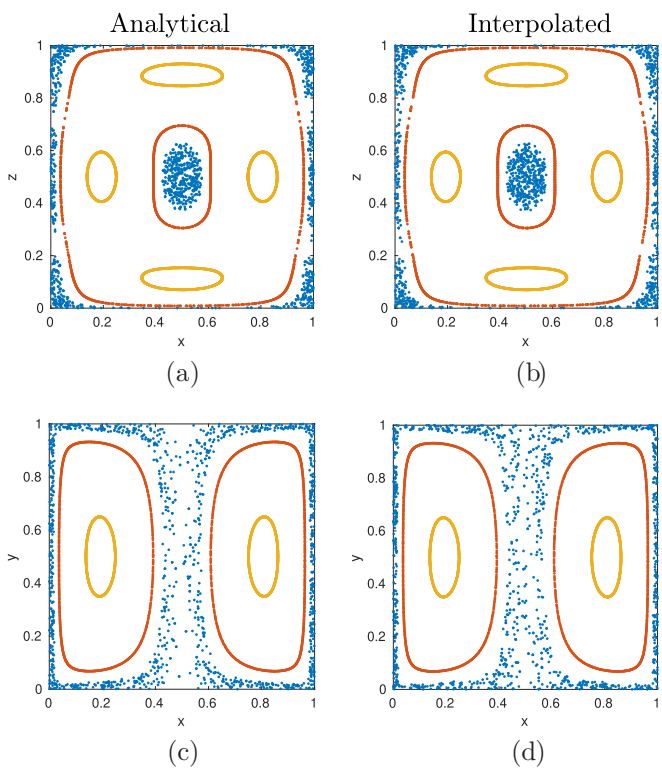

FIG. 11. Poincaré sections in different planes for the analytic flow obtained for $U_1 = 0.5$ and $U_2 = 0.346$. The top views concern the xz plane at mid-y and the bottom views the xy plane at mid-z. Three trajectories have been calculated to get these Poincaré sections, initiated from the points (0.01, 0.01, 0.01) (blue dots), (0.1, 0.1, 0.1) (red dots), and (0.3, 0.3, 0.3) (orange dots). Left column (a)–(c): Trajectories obtained from analytic velocity values; right column (b)–(d): Trajectories obtained from velocity values interpolated from values stored on a grid ($41 \times 61 \times 61$ points).

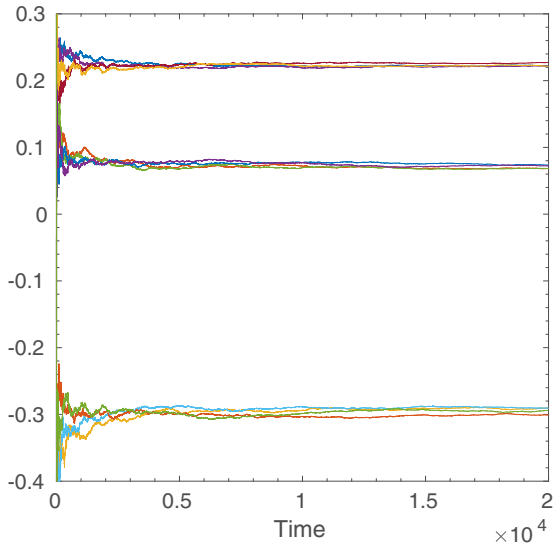

FIG. 12. Lyapunov exponents obtained with trajectories issued from the initial point (0.2, 0.2, 0.2) for two analytic oscillatory flows with $U_1 = 0.25$ and $U_2 = 0.387$ (see text) and with flow velocities obtained either analytically or by interpolation from values stored in time (150 fields in the period) and on a grid of $41 \times 61 \times 61$ points.

APPENDIX A: VALIDATION OF THE CALCULATION OF TRAJECTORIES FOR 3D STEADY FLOWS

To validate the interpolation on the parallelepipedic lattice, we used a 3D analytical stationary flow in a cubic $1 \times 1 \times 1$ cavity (coordinates from 0 to 1 in each direction), which exhibits chaotic advection [64]:

$$v_x = -U_1 \sin \pi x \cos \pi z, \tag{A1}$$

$$v_y = -2\, U_2 \sin \pi y \cos 2\pi z, \tag{A2}$$

$$v_z = U_1 \cos \pi x \sin \pi z + U_2 \cos \pi y \sin 2\pi z. \tag{A3}$$

For the case of nonglobal chaos $U_1 = 0.5$ and $U_2 = 0.346$, we have calculated trajectories on a time interval of 5000 with a time step $dt = 0.1$. The solver of MATLAB ode45 adapts its own time step to get a precision of 10^{-6}. The trajectories are used to calculate the Lyapunov exponents (Wolf method) and to get Poincaré sections in the three principal planes. Moreover, in view of testing the fair accuracy of the interpolation on a grid, the trajectories are obtained on one side from analytic velocity values and on another side from velocity values interpolated from stored values on a grid of $41 \times 61 \times 61$ points, the same grid as in the numerical simulations of acoustic streaming. Poincaré sections obtained in each case are shown in Fig. 11. For both Poincaré sections, the comparison is very good, with results which are also similar to what was obtained in Ref. [64], validating the calculation of trajectories and the space interpolation process. Note that the Lyapunov exponents obtained are also in accordance with the values given in Ref. [64].

APPENDIX B: VALIDATION OF THE CALCULATION OF TRAJECTORIES FOR 3D OSCILLATORY PERIODIC FLOWS

We have generated an analytic oscillatory flow from the analytic stationary flow used in the previous section, but with the choice of $U_1 = 0.25$ and $U_2 = 0.387$ corresponding to globally

chaotic trajectories. To obtain three nonzero Lyapunov exponents, we have chosen a period $T = 3$ divided in three different phases with equal duration $T_p = 1$. For the first part, we choose the usual steady flow; for the second part, the same flow with a first permutation of the axes, and for the third part, the flow obtained after a new permutation of the axes, see Ref. [65]. Because this flow changes abruptly between each phase, we also introduced a smoother oscillatory flow, obtained by multiplying the flow in each phase by $\sin^2(\pi\, t/T_p)/2$. As the integral of $\sin^2(\pi\, t/T_p)/2$ for t between 0 and T_p is equal to 1, both oscillatory fields ought to give equivalent displacements of the fluid particles by the flow and then equivalent Lyapunov exponents. On these examples, we have tested the interpolations in both space and time. Indeed, we have calculated the trajectories and the Lyapunov exponents on one side from the analytic velocity values and on the other side from velocity values interpolated from stored values taken at 50 times during each phase of the period and on a grid of $41 \times 61 \times 61$ points. The Lyapunov exponents obtained in these different cases are shown in Fig. 12. We see that, for both oscillatory flows, the Lyapunov exponents obtained after a time $t = 20\,000$, either analytically or with interpolations, are very similar and correspond to what is expected in such situation [65]. This validates the time and space interpolation process.

[1] H. Monnier, A. M. Wilhelm, and H. Delmas, Effects of ultrasound on micromixing in flow cell, Chem. Eng. Sci. **55**, 4009 (2000).

[2] Z. Yang, S. Matsumoto, H. Goto, M. Matsumoto, and R. Maeda, Ultrasonic micromixer for microfluidic systems, Sens. Actuators, A **93**, 266 (2001).

[3] Y. Ito, K. Nagata, and S. Komori, The effects of high-frequency ultrasound on turbulent liquid mixing with a rapid chemical reaction, Phys. Fluids **14**, 4362 (2002).

[4] Nasrul Fikry Che Pa, N. L. Chin, Y. A. Yusof, and N. Abdul Aziz, Power ultrasound assisted mixing effects on bread physical properties, Agric. Agric. Sci. Procedia **2**, 60 (2014).

[5] R. S. Davidson, A. Safdar, J. D. Spencer, and B. Robinson, Applications of ultrasound to organic chemistry, Ultrasonics **25**, 35 (1987).

[6] S. A. Endaylalu and W.-H. Tien, Mixing enhancement in T-junction microchannel with acoustic streaming induced by triangular structure, Biomicrofluidics **15**, 034102 (2021).

[7] C. Pothuri, M. Azharudeen, and K. Subramani, Rapid mixing in microchannel using standing bulk acoustic waves, Phys. Fluids **31**, 122001 (2019).

[8] C. Eckart, Vortices and streams caused by sound waves, Phys. Rev. **73**, 68 (1948).

[9] S. J. Lighthill, Acoustic streaming, J. Sound Vib. **61**, 391 (1978).

[10] W. L. Nyborg, Acoustic streaming, in *Properties of Polymers and Nonlinear Acoustics*, Physical Acoustics, Vol. 2, edited by Warren P. Mason (Academic Press Inc., New York, 1965), pp. 265–331.

[11] K. D. Frampton, S. E. Martin, and K. Minor, The scaling of acoustic streaming for application in microfluidic devices, Appl. Acoust. **64**, 681 (2003).

[12] B. Moudjed, V. Botton, D. Henry, H. Ben Hadid, and J.-P. Garandet, Scaling and dimensional analysis of acoustic streaming jets, Phys. Fluids **26**, 093602 (2014).

[13] R. Ben Haj Slama, B. Gilles, M. Ben Chiekh, and J.-C. Béra, PIV for the characterization of focused field induced acoustic streaming: Seeding particle choice evaluation, Ultrasonics **76**, 217 (2017).

[14] J. S. Marshall and J. Wu, Acoustic streaming, fluid mixing, and particle transport by a gaussian ultrasound beam in a cylindrical container, Phys. Fluids **27**, 103601 (2015).

[15] A. Green, J. S. Marshall, D. Ma, and J. Wu, Acoustic streaming and thermal instability of flow generated by ultrasound in a cylindrical container, Phys. Fluids **28**, 104105 (2016).

[16] C. Suri, K. Takenaka, H. Yanagida, Y. Kojima, and K. Koyama, Chaotic mixing generated by acoustic streaming, Ultrasonics **40**, 393 (2002).

[17] S. Dumitrica, D. Vizman, J.-P. Garandet, and A. Popescu, Numerical studies on a type of mechanical stirring in directional solidification method of multicrystalline silicon for photovoltaic applications, J. Cryst. Growth **360**, 76 (2012).

[18] M. Chatelain, V. Botton, M. Albaric, D. Pelletier, B. Cariteau, D. Abdo, and M. Borrelli, Mechanical stirring influence on solute segregation during plane front directional solidification, Int. J. Therm. Sci. **126**, 252 (2018).

[19] B. Moudjed, V. Botton, D. Henry, S. Millet, and H. Ben Hadid, Y-shaped jets driven by an ultrasonic beam reflecting on a wall, Ultrasonics **68**, 33 (2016).

[20] N. El Ghani, S. Miralles, V. Botton, D. Henry, H. Ben Hadid, B. Ter-Ovanessian, and S. Marcelin, Acoustic streaming enhanced mass transfer at a wall, Int. J. Heat Mass Transf. **172**, 121090 (2021).

[21] T. Cambonie, B. Moudjed, V. Botton, D. Henry, and H. Ben Hadid, From flying wheel to square flow: Dynamics of a flow driven by acoustic forcing, Phys. Rev. Fluids **2**, 123901 (2017).

[22] G. Launay, T. Cambonie, D. Henry, A. Pothérat, and V. Botton, Transition to chaos in an acoustically driven cavity flow, Phys. Rev. Fluids **4**, 044401 (2019).

[23] H. Aref, Stirring by chaotic advection, J. Fluid Mech. **143**, 1 (1984).

[24] T. Dombre, U. Frisch, J. M. Greene, M. Hénon, A. Mehr, and A. M. Soward, Chaotic streamlines in the ABC flows, J. Fluid Mech. **167**, 353 (1986).

[25] J. M. Ottino, *The Kinematics of Mixing: Stretching, Chaos and Transport* (Cambridge University Press, New-York, 1989).

[26] V. Rom-Kedar, A. Leonard, and S. Wiggins, An analytical study of the transport, mixing and chaos in an unsteady vortical flow, J. Fluid Mech. **214**, 347 (1990).

[27] S. Wiggins and J. M. Ottino, Foundations of chaotic mixing, Phil. Trans. R. Soc. Lond A **362**, 937 (2004).

[28] E. Gouillart, J.-L. Thiffeault, and M. D. Finn, Topological mixing with ghost rods, Phys. Rev. E **73**, 036311 (2006).

[29] A. Figueroa, P. Meunier, S. Cuevas, E. Villermaux, and E. Ramos, Chaotic advection at large Péclet number: Electromagnetically driven experiments, numerical simulations, and theoretical predictions, Phys. Fluids **26**, 013601 (2014).

[30] P. Meunier, P. Huck, C. Nobili, and E. Villermaux, Experimental measurement of the Melnikov function, Phys. Fluids **27**, 077103 (2015).

[31] H. Aref, J. R. Blake, M. Budišić, S. S. S. Cardoso, J. H. E. Cartwright, H. J. H. Clercx, K. El Omari, U. Feudel, R. Golestanian, E. Gouillart, G. F. van Heijst, T. S. Krasnopolskaya, Y. Le Guer, R. S. MacKay, V. V. Meleshko, G. Metcalfe, I. Mezić, A. P. S. de Moura, O. Piro, M. F. M. Speetjens, R. Sturman, J.-L. Thiffeault *et al.*, Frontiers of chaotic advection, Rev. Mod. Phys. **89**, 025007 (2017).

[32] L. D. Smith, P. B. Umbanhowar, R. M. Lueptow, and J. M. Ottino, The geometry of cutting and shuffling: An outline of possibilities for piecewise isometries, Phys. Rep. **802**, 1 (2019).

[33] K. El Omari, E. Younes, T. Burghelea, C. Castelain, Y. Moguen, and Y. Le Guer, Active chaotic mixing in a channel with rotating arc-walls, Phys. Rev. Fluids **6**, 024502 (2021).

[34] M. F. M. Speetjens, H. J. H. Clercx, and G. J. F. Van Heijst, A numerical and experimental study on advection in three-dimensional Stokes flows, J. Fluid Mech. **514**, 77 (2004).

[35] K. Ngan and J. Vanneste, Scalar decay in a three-dimensional chaotic flow, Phys. Rev. E **83**, 056306 (2011).

[36] N. R. Moharana, M. F. M. Speetjens, R. R. Trieling, and H. J. H. Clercx, Three-dimensional Lagrangian transport phenomena in unsteady laminar flows driven by a rotating sphere, Phys. Fluids **25**, 093602 (2013).

[37] C. Habchi, J. L. Harion, S. Russeil, D. Bougeard, F. Hachem, and A. Elmarakbi, Chaotic mixing by longitudinal vorticity, Chem. Eng. Sci. **104**, 439 (2013).

[38] P. Meunier, Geoinspired soft mixers, J. Fluid Mech. **903**, A15 (2020).

[39] A. D. Stroock, S. K. W. Dertinger, A. Ajdari, I. Mezic, H. A. Stone, and G. M. Whitesides, Chaotic mixer for microchannels, Science **295**, 647 (2002).

[40] H. A. Stone, A. D. Stroock, and A. Ajdari, Engineering flows in small devices: Microfluidics toward lab-on-a-chip, Annu. Rev. Fluid Mech. **36**, 381 (2004).

[41] F. Raynal, A. Beuf, and P. Carrière, Numerical modeling of DNA-chip hybridization with chaotic advection, Biomicrofluidics **7**, 034107 (2013).

[42] H. Peerhossaini, C. Castelain, and Y. Le Guer, Heat exchanger design based on chaotic advection, Exp. Therm. Fluid Sci. **7**, 333 (1993).

[43] M. Creyssels, S. Prigent, Y. Zhou, X. Jianjin, C. Nicot, and P. Carrière, Laminar heat transfer in the 'MLLM' static mixer, Int. J. Heat Mass Transf. **81**, 774 (2015).

[44] S. Amir Bahrani, L. Humberset, R. Osipian, L. Royon, K. Azzouz, and A. Bontemps, How thermally efficient are chaotic advection mixers? An experimental assessment, Int. J. Therm. Sci. **145**, 106046 (2019).

[45] P. B. Rhines and W. R. Young, How rapidly is a passive scalar mixed within closed streamlines? J. Fluid Mech. **133**, 133 (1983).

[46] F. Raynal and J.-N. Gence, Energy saving in chaotic laminar mixing, Int. J. Heat Mass Transf. **40**, 3267 (1997).

[47] When considering mixing and, in particular, chaotic advection, a nonsymmetric flow always enhances mixing [66]. However, our aim here is to study mixing in connection with photovoltaic crystal growth configurations, where the solid-liquid front rises with time. Therefore, even if the acoustic source is located in the upper part at initial time, there comes a moment when it is located at midheight. Choosing the most unfavorable location ensures that mixing will be efficient during the whole process.

[48] D. T. Blackstock, *Fundamental of Physical Acoustics* (Wiley-Interscience, New York, 2000).

[49] H. Ben Hadid and D. Henry, Numerical study of convection in the horizontal Bridgman configuration under the action of a constant magnetic field. Part 2. Three-dimensional flow, J. Fluid Mech. **333**, 57 (1997).

[50] F. Raynal and S. Wiggins, Lobe dynamics in a kinematic model of a meandering jet. I. Geometry and statistics of transport and lobe dynamics with accelerated convergence, Physica D **223**, 7 (2006).

[51] E. Gouillart, N. Kuncio, O. Dauchot, B. Dubrulle, S. Roux, and J.-L. Thiffeault, Walls Inhibit Chaotic Mixing, Phys. Rev. Lett. **99**, 114501 (2007).

[52] E. Gouillart, O. Dauchot, B. Dubrulle, S. Roux, and J.-L. Thiffeault, Slow decay of concentration variance due to no-slip walls in chaotic mixing, Phys. Rev. E **78**, 026211 (2008).

[53] F. Raynal and P. Carrière, The distribution of "time of flight" in three dimensional stationary chaotic advection, Phys. Fluids **27**, 043601 (2015).

[54] B. Kadoch, W. J. T. Bos, and K. Schneider, Efficiency of laminar and turbulent mixing in wall-bounded flows, Phys. Rev. E **101**, 043104 (2020).

[55] R. Artuso, L. Cavallasca, and G. Cristadoro, Dynamical and transport properties in a family of intermittent area-preserving maps, Phys. Rev. E **77**, 046206 (2008).

[56] F. Raynal and J.-N. Gence, Efficient stirring in planar, time-periodic laminar flows, Chem. Eng. Sci. **50**, 631 (1995).

[57] A. Pumir, A numerical study of the mixing of a passive scalar in three dimensions in the presence of a mean gradient, Phys. Fluids **6**, 2118 (1994).

[58] See Supplemental Material at http://link.aps.org/supplemental/10.1103/PhysRevFluids.7.064501 for a video of mixing of a small blob of dye at $A = 10^6$.

[59] See Supplemental Material at http://link.aps.org/supplemental/10.1103/PhysRevFluids.7.064501 for a video of mixing of a small blob of dye at $A = 1.5 \times 10^6$.

[60] See Supplemental Material at http://link.aps.org/supplemental/10.1103/PhysRevFluids.7.064501 for a video of mixing of a small blob of dye at $A = 2.4 \times 10^6$.

[61] In the videos, t_{macro} corresponds to the video time $t_v = 35$ s for the steady case at $A = 10^6$ (2 frames/s), and $t_v = 30$ s and 20 s, respectively, for the oscillatory cases at $A = 1.5 \times 10^6$ and 2.4×10^6 (1 frame/s). Note the very rapid changes, with a wide spreading of the blob particles, which occur just before and after those times.

[62] M. Petrelli, K. El Omari, Y. Le Guer, and D. Perugini, Effects of chaotic advection on the timescales of cooling and crystallization of magma bodies at mid crustal levels, Geochem., Geophys., Geosyst. **17**, 425 (2016).

[63] J. Hofstetter, J. F. Lelièvre, C. Del Cañizo, and A. del Luque, Acceptable contamination levels in solar grade silicon: From feedstock to solar cell, Mater. Sci. Eng. B **159-160**, 299 (2009).

[64] V. Toussaint, P. Carrière, and F. Raynal, A numerical Eulerian approach to mixing by chaotic advection, Phys. Fluids **7**, 2587 (1995).

[65] G. Pillet, S. Fauve, and F. Raynal, Backwards mixing (2020), https://hal.archives-ouvertes.fr/hal-02426167.

[66] A. Beuf, J.-N. Gence, P. Carrière, and F. Raynal, Chaotic mixing efficiency in different geometries of Hele-Shaw cells, Int. J. Heat Mass Transf. **53**, 684 (2010).